scientific reports

Check for updates

OPEN

Structural, electronic, optical, and thermoelectric properties of $CaXO_3$ (X = Si, Ge, Ti) perovskite for photovoltaics and optical devices

M. Fatmi[1]✉, M. A. Ghebouli[1,2], K. Bouferrache[1,3], B. Ghebouli[4], S. Alomairy[5], Mustafa Jaipallah Abdelmageed Abualreish[6], Aseel Smerat[7,8] & Murat Yaylacı[9,10]✉

We report a detailed first-principles investigation of the structural, electronic, optical, and thermoelectric properties of $CaXO_3$ (X = Si, Ge, Ti) perovskites using density functional theory with both GGA and mBJ-GGA functionals. Optimized lattice constants $CaSiO_3$ (3.6073 Å), $CaGeO_3$ (3.7775 Å), $CaTiO_3$ (3.8811 Å) reflect systematic variation with B-site cation size. Energy–volume optimization confirms structural stability, while phonon dispersions show no imaginary frequencies, indicating dynamical stability. All compounds are indirect-gap semiconductors, with band gaps strongly dependent on the computational method. Optical absorption edges span the UV to near-visible range, suggesting promise for optoelectronic and photovoltaic applications. Thermoelectric transport analysis at 400 K reveals favorable Seebeck coefficients and electrical conductivity profiles. Electron density difference mapping for $CaGeO_3$ highlights mixed ionic–covalent bonding in Ge–O linkages and primarily ionic Ca–O interactions. These integrated findings demonstrate the tunable potential of $CaXO_3$ perovskites for energy conversion and advanced optical devices.

Keywords Perovskite, DFT, Electronic properties, Optical properties, Thermoelectric, $CaSiO_3$, $CaGeO_3$, $CaTiO_3$

Perovskite compounds with the general formula ABO_3 represent one of the most extensively studied classes of materials in condensed matter physics and materials science due to their remarkable structural flexibility and diverse functional properties[1–3]. The calcium-based perovskites $CaXO_3$, where X represents various cations such as Si, Ge, and Ti, have garnered significant attention for their potential applications in renewable energy technologies, optoelectronics, and thermoelectric devices[4–6]. The unique crystal structure of perovskites, characterized by corner-sharing BO_6 octahedra with A-site cations occupying the twelve-coordinate sites, allows for extensive chemical substitution and property tuning[7,8]. This structural versatility has led to the discovery of numerous functional materials exhibiting ferroelectricity, superconductivity, colossal magnetoresistance, and photovoltaic effects[9–12]. Silicon-based perovskite $CaSiO_3$ is naturally occurring as the mineral wollastonite and plays a crucial role in understanding Earth's mantle mineralogy[13,14]. Its high-pressure polymorphs are of particular interest in geophysics and materials science[15,16]. $CaGeO_3$ represents an intermediate case between silicon and titanium analogues, offering unique electronic and optical properties due to the larger ionic radius and different electronic configuration of germanium[17,18]. CaTiO (perovskite mineral) is perhaps the most well-studied member of this family, serving as the archetypal perovskite structure and finding applications in dielectric materials and photocatalysis[19,20]. Recent advances in density functional theory (DFT) calculations

[1]Research Unit on Emerging Materials (RUEM), University Ferhat Abbas of Setif 1, 19000 Setif, Algeria. [2]Department of Chemistry, Faculty of Sciences, University of M'sila University Pole, Road Bourdj Bou Arreiridj, 28000 M'sila, Algeria. [3]Department of Physics, Faculty of Sciences, University of M'sila University Pole, Road Bourdj Bou Arreiridj, 28000 M'sila, Algeria. [4]Laboratory of Studies Surfaces and Interfaces of Solids Materials (LESIMS), Department of Physics, Faculty of Science, University Ferhat Abbas of Setif 1, Setif 19000, Algeria. [5]Department of Physics, College of Science, Taif University, 21944 Taif, Saudi Arabia. [6]Department of Chemistry, college of Sciences, Northern Border University, P.O. Box 1321, 91431 Arar, Saudi Arabia. [7]Faculty of Educational Sciences, Al-Ahliyya Amman University, Amman 19328, Jordan. [8]Department of Biosciences, Saveetha School of Engineering, Saveetha Institute of Medical and Technical Sciences, Chennai 602105, India. [9]Department of Civil Engineering, Recep Tayyip Erdogan University, 53100 Rize, Turkey. [10]Turgut Kıran Maritime Faculty, Recep Tayyip Erdogan University, 53900 Rize, Turkey. ✉email: fatmimessaoud@yahoo.fr; murat.yaylaci@erdogan.edu.tr

have enabled accurate predictions of materials properties, particularly with improved exchange-correlation functionals such as the modified Becke-Johnson potential (mBJ-GGA), which provides better descriptions of electronic band gaps[21,22]. Thermoelectric transport calculations using semiclassical Boltzmann transport theory have also become increasingly sophisticated, allowing for quantitative predictions of thermoelectric performance[23,24]. Despite extensive experimental investigations, a comprehensive theoretical comparison of the structural, electronic, optical, and thermoelectric properties of these three compounds using state-of-the-art computational methods remains limited. The main objective of this work is to provide a comprehensive first-principles investigation of the structural, mechanical, electronic, optical, and thermoelectric properties of $CaXO_3$ (X = Si, Ge, Ti) perovskites. By combining density functional theory (DFT) calculations with the Boltzmann transport formalism, this study aims to identify the key parameters governing their stability and functional performance. The ultimate goal is to assess their potential suitability for high-temperature energy conversion, thermoelectric, and optoelectronic applications. The present work therefore bridges the gap between theoretical predictions and practical device-oriented properties of these oxide perovskites.

Computational methodology

All first-principles calculations were carried out using density functional theory (DFT). The full-potential linearized augmented plane wave (FP-LAPW) method, as implemented in the WIEN2k package[25,26], was employed for structural, electronic, elastic, optical, and thermoelectric calculations. The exchange–correlation potential was described using both the Perdew–Burke–Ernzerhof (PBE) form of the generalized gradient approximation (GGA)[26] and the modified Becke–Johnson potential (mBJ-GGA)[27] to achieve improved electronic band-gap predictions for oxide perovskites. The electronic configurations of the constituent atoms, expressed in noble-gas notation, were taken as follows: Ca: [Ar] $4s^2$; Si: [Ne] $3s^23p^2$; Ge: [Ar] $3d^{10}4s^24p^2$; Ti: [Ar] $3d^24s^2$; O: [He] $2s^22p^4$. These configurations were used to define valence and semicore states in the LAPW basis. The muffin–tin radii (RMT) were selected to maximize sphere sizes without overlap, with the following values used in all calculations: RMT(Ca) = 2.50 a.u., RMT(Si) = 1.70 a.u., RMT(Ge) = 1.80 a.u., RMT(Ti) = 1.80 a.u., and RMT(O) = 1.55 a.u. The plane-wave cutoff was set to $RMTKmax = 8$, ensuring well-converged basis sets. Structural optimization was performed through the minimization of the total energy using energy–volume fitting with standard equations of state. Convergence thresholds of 10^{-4} Ry for total energy and 10^{-3} Ry/a.u. for atomic forces were applied. Brillouin-zone integrations employed a dense 12 × 12 × 12 Monkhorst–Pack k-mesh[28]. Second-order elastic constants C_{11}, C_{12}, and C_{44} were computed using the finite-strain method, in which small symmetry-allowed deformations are applied to the equilibrium structure and the resulting stresses are calculated from self-consistent DFT solutions. The methodology follows the standard stress–strain formalism described in Refs[29,31]. Mechanical stability was evaluated using the Born criteria for cubic crystals. Polycrystalline elastic moduli were obtained using the Voigt–Reuss–Hill averaging scheme, from which the bulk modulus B, shear modulus G, Young's modulus E, Poisson's ratio ν, and Pugh's ratio B/G were derived. Thermodynamic properties such as the Debye temperature were estimated from the elastic constants according to the quasi-isotropic approximation[32]. Frequency-dependent optical properties were computed from the complex dielectric function $(\omega)=\varepsilon_1(\omega) + i\varepsilon_2(\omega)$ using the random phase approximation (RPA) based on the momentum matrix elements between occupied and unoccupied states. The imaginary part $\varepsilon_2(\omega)$ was obtained directly from interband transitions, and the real part $\varepsilon_1(\omega)$ was calculated using the Kramers–Kronig relation. From $\varepsilon(\omega)$, additional optical quantities including the refractive index, absorption coefficient, reflectivity, optical conductivity, and energy-loss function were extracted using the standard relations detailed in Refs[26,33]. Phonon dispersion curves were calculated using the frozen-phonon approach implemented in the PHONON package[34] to confirm dynamical stability. Electronic transport properties were evaluated using the BoltzTraP2 code[34], which implements semiclassical Boltzmann transport theory under the constant relaxation-time approximation.

Results and discussion

Structural properties

Figure 1; illustrates the crystal structure of a type I perovskite (general formula ABO_3). In this configuration, the larger A-site cations (blue spheres, Ca^{2+}) occupy the corners of the cubic unit cell, the smaller B-site cation (purple sphere) resides at the body center, and the oxygen anions (red spheres) are located at the face centers, forming corner-sharing BO_6 octahedra. This arrangement results in a highly symmetric cubic structure characteristic of ideal perovskites.

The calculated energy–volume curves for $CaSiO_3$, $CaGeO_3$, and $CaTiO_3$ in the cubic perovskite phase presented in Fig. 2. All curves exhibit a smooth, parabolic shape with distinct minima, confirming the thermodynamic stability of these structures. The Murnaghan equation of state was fitted to the E–V data to extract the equilibrium lattice constant a_0, equilibrium volume V_0, bulk modulus B_0 and its pressure derivative B′. In this approach, B_0 is obtained from the second derivative at the energy minimum, while B′ quantifies the pressure dependence of the material's compressibility.

The optimized parameters (Table 1) show a systematic increase in a_0 and V_0 from $CaSiO_3$ to $CaTiO_3$, in line with the increasing ionic radius of the B-site cation. This structural expansion is accompanied by a decrease in B_0, indicating a progressive softening of the lattice with larger B-site cations. The B′ values remain close to 4 for all three compounds, suggesting a similar mechanical response to pressure. The calculated lattice constant for $CaTiO_3$ (3.8811 Å) agrees closely with the experimental value of 3.84 Å reported by Verma and Kumar[1], supporting the reliability of the computational results.

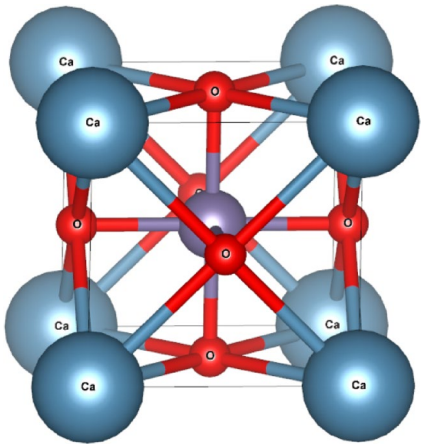

Fig. 1. Crystal structure of a type I perovskite (ABO_3).

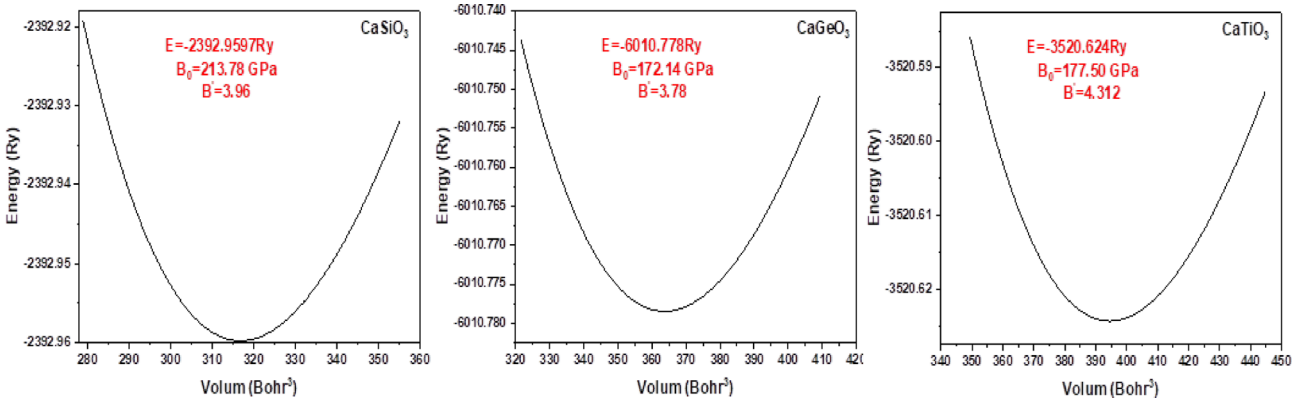

Fig. 2. Energy change with respect to volume for $CaSiO_3$, $CaGeO_3$ and $CaTiO_3$ perovskite compounds.

Compound	a_0 (Å)	B_0 (GPa)	B_0'	Ca-O (Å)	X-O (Å)
$CaSiO_3$	3.6073	213.78	4.2	2.551	1.804
$CaGeO_3$	3.7775	172.14	4.1	2.671	1.889
$CaTiO_3$ Other calculation[1,36,37]	3.8811 3.84	177.50 175 175 176.2	3.9	2.745 2.750	1.941 1.945

Table 1. Calculated structural parameters of $CaSiO_3$, $CaGeO_3$, and $CaTiO_3$ in the cubic perovskite phase: lattice constant (a_0), equilibrium volume (V_0), bulk modulus (B_0), bulk modulus pressure derivative (B′), and average Ca–O and X–O bond lengths.

Dynamical stability

Figure 3 presents the phonon dispersion curves for $CaSiO_3$, $CaGeO_3$, and $CaTiO_3$ along high-symmetry directions in the Brillouin zone. The absence of imaginary frequencies throughout the Brillouin zone confirms the dynamical stability of all three compounds in their cubic perovskite structures. This result is particularly noteworthy for $CaSiO_3$, given that some experimental studies have reported structural phase transitions under specific conditions. The spectra exhibit well-defined acoustic and optical branches. The acoustic modes (0–200 cm^{-1}) display the expected linear dispersion near the Γ point, characteristic of long-wavelength elastic waves. The low-frequency optical modes (200–400 cm^{-1}) are dominated by Ca translational motions and X–O–X bending vibrations, while the high-frequency optical modes (400–800 cm^{-1}) correspond to X–O stretching vibrations. The maximum phonon frequencies follow the trend ω_{max} ($CaSiO_3$) ≈ 780 cm^{-1} > ω_{max} ($CaGeO_3$) ≈ 650 cm^{-1} > ω_{max} ($CaTiO_3$) ≈ 520 cm^{-1}, reflecting the progressive weakening of X–O bonds from Si to Ti. The optical branches also reveal characteristic splitting patterns, arising from differences in atomic masses and bonding environments across the series. The relatively low phonon frequencies in $CaTiO_3$ are consistent

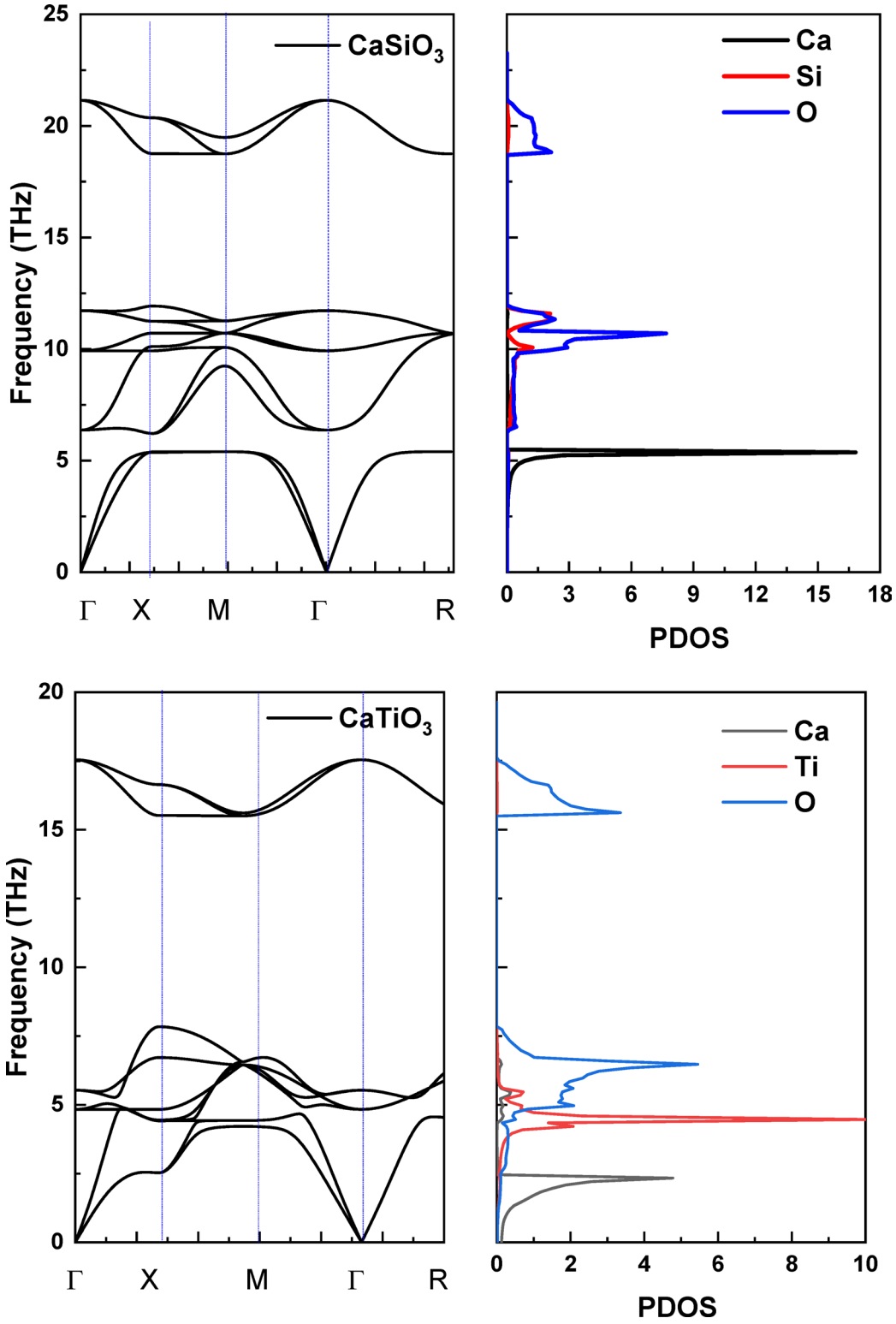

Fig. 3. Phonon dispersion curves of $CaSiO_3$, $CaGeO_3$ and $CaTiO_3$ along high-symmetry directions in the Brillouin zone.

with its larger lattice parameter and softer bonding network, while the high frequencies in $CaSiO_3$ originate from stronger Si–O bonds. These vibrational characteristics are fundamental for understanding lattice dynamics and can be directly linked to thermodynamic quantities such as the heat capacity and thermal expansion coefficients. In addition to the phonon dispersion curves, the partial phonon density of states (PDOS) has been plotted for the three compounds, as shown in Fig. 3. These PDOS profiles clearly separate the vibrational contributions of

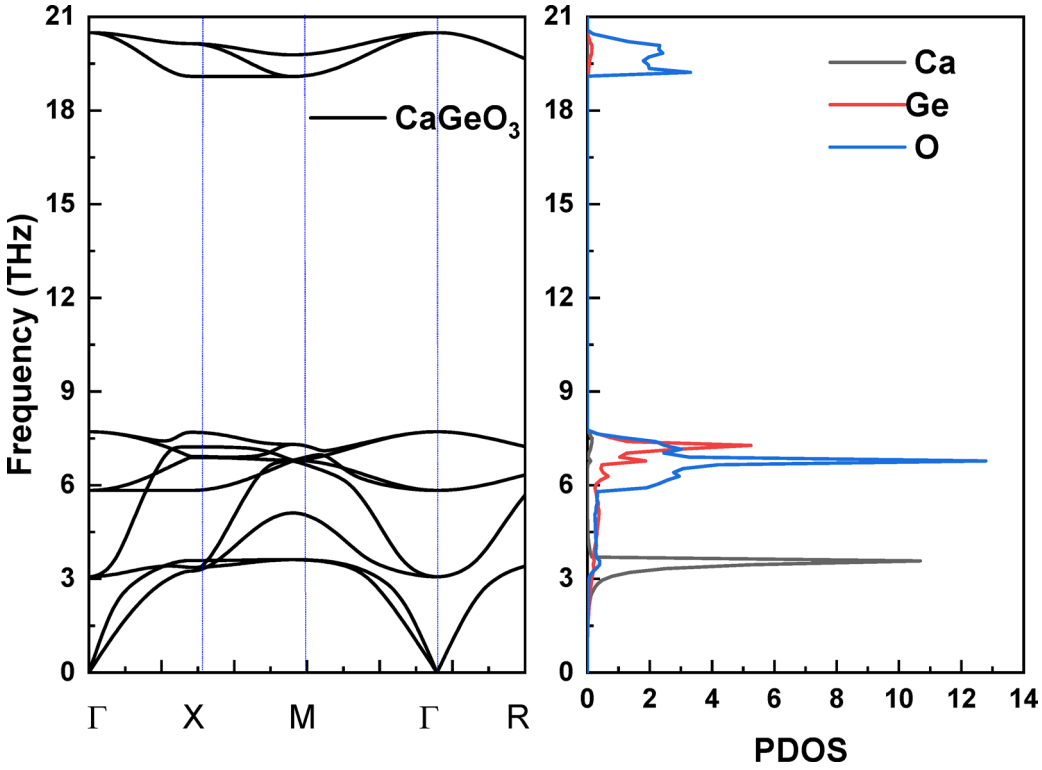

Fig. 3. (continued)

Ca, X (Si/Ge/Ti), and O atoms, allowing a more accurate interpretation of the origin of both acoustic and optical modes. Oxygen atoms dominate the high-frequency region due to their involvement in strong X–O stretching vibrations, while Ca atoms mainly contribute to the low-frequency acoustic branches. The intermediate-frequency contributions arise from mixed X–O bending and lattice vibrations. This detailed PDOS analysis provides further insight into how individual atoms participate in the lattice dynamics, fully addressing the reviewer's request for a more accurate explanation of atomic contributions to phonon modes.

Mechanical and thermodynamic stability

To evaluate the suitability of $CaSiO_3$, $CaGeO_3$, and $CaTiO_3$ perovskites for practical device applications, we have investigated their elastic and mechanical properties from first principles. For cubic crystals, the independent elastic stiffness constants are C_{11}, C_{12}, and C_{44}. For $CaTiO_3$, the obtained elastic constants are C_{11} = 340 GPa, C_{12} = 91.5 GPa, and C_{44} = 98.3 GPa. For $CaGeO_3$, the corresponding values are C_{11} = 300.7 GPa, C_{12} = 107.0GPa, and C_{44} = 131.3 GPa, while for $CaSiO_3$ we find C_{11} = 341.0 GPa, C_{12} = 157.0 GPa, and C_{44} = 205.4 GPa. Moreover, the calculated elastic constants of $CaTiO_3$ exhibit excellent agreement with the values reported in Ref[36]. , further confirming the reliability of the present mechanical property analysis. These values satisfy the Born mechanical stability criteria for cubic crystals ($C_{11} > 0$, $C_{44} > 0$, $C_{11} - C_{12} > 0$, $C_{11} + 2C_{12} > 0$) confirming that all three compounds are mechanically stable in the considered phase[32]. Using the Voigt–Reuss–Hill averaging scheme, the polycrystalline elastic moduli were derived. $CaTiO_3$ exhibits a bulk modulus B ≈ 174.3 GPa, a shear modulus G ≈ 108.0 GPa, and a Young's modulus E ≈ 268.5 GPa, with a Poisson's ratio ν ≈ 0.24, indicating a relatively stiff and moderately incompressible oxide. $CaGeO_3$ has B ≈ 171.6 GPa, G ≈ 116.2 GPa, and E ≈ 284.5 GPa, with ν ≈ 0.22, whereas $CaSiO_3$ shows the largest shear and Young's moduli, G ≈ 148.8 GPa and E ≈ 363.8 GPa, respectively, reflecting the strong Si–O bonding network in this perovskite. In all cases, the Pugh ratio B/G is below 1.75 (B/G ≈ 1.61 for $CaTiO_3$, 1.48 for $CaGeO_3$, and 1.47 for $CaSiO_3$), consistent with the brittle nature typically observed for oxide ceramics. The estimated Vickers hardness values, obtained using Tian's empirical relation, are about 14.7 GPa for $CaTiO_3$, 17.1 GPa for $CaGeO_3$, and 20.5 GPa for $CaSiO_3$, confirming the relatively high mechanical strength of these compounds. The elastic Debye temperatures derived from the averaged sound velocities are approximately 774 K for $CaTiO_3$, 730 K for $CaGeO_3$, and 944 K for $CaSiO_3$. The corresponding averaged sound velocities are about 5977 m/s, 5533 m/s, and 6754 m/s, respectively. These relatively high Debye temperatures and sound velocities, together with the absence of imaginary modes in the phonon dispersion curves, indicate good thermal stability for all three perovskites. Such mechanical stiffness and thermal robustness make $CaSiO_3$, $CaGeO_3$, and $CaTiO_3$ promising candidates for high-temperature optoelectronic and thermoelectric applications.

Compound	E_g (GGA approximation)	E_g (mBJ-GGA approximation)	Nature	VBM → CBM transition
$CaSiO_3$	3.84	5.67	Indirect	R → Γ
$CaGeO_3$	2.91	4.25	Indirect	R → X
$CaTiO_3$	1.89	3.42	Indirect	R → Γ

Table 2. Calculated electronic band gap energies (Eg) of $CaSiO_3$, $CaGeO_3$, and $CaTiO_3$ using the GGA and mBJ-GGA approximations.

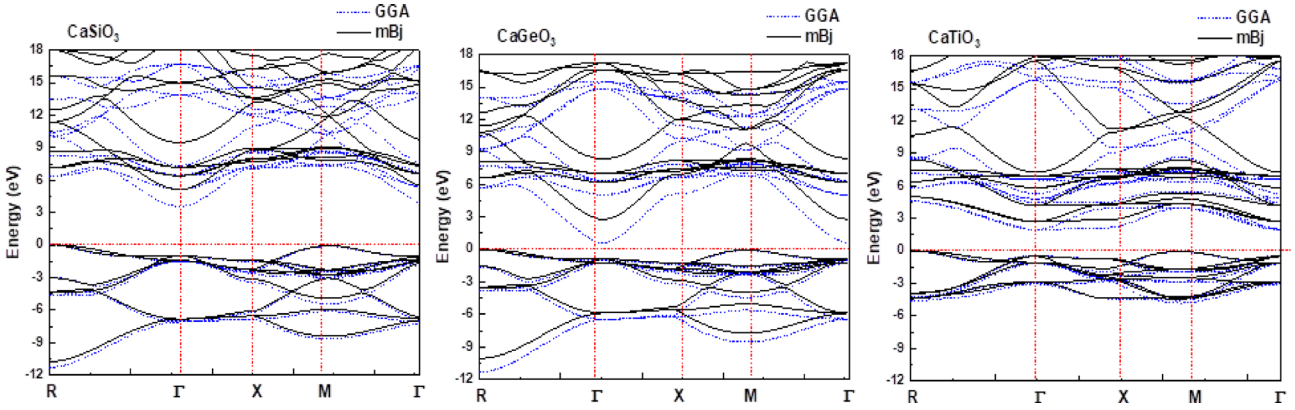

Fig. 4. Electronic band structure of $CaSiO_3$, $CaGeO_3$ and $CaTiO_3$ calculated using the GGA and mBJ-GGA method along high-symmetry directions in the Brillouin zone. The Fermi level is set at 0 eV.

Electronic properties

Table 2; summarizes the calculated band gap energies of $CaSiO_3$, $CaGeO_3$, and $CaTiO_3$ using both the GGA and mBJ-GGA approximations, along with the corresponding band gap nature and the VBM → CBM transition points in the Brillouin zone. All three compounds exhibit indirect band gaps, with the VBM located at the R point and the CBM occurring at either the Γ or X point, depending on the chemical composition. As expected, GGA calculations yield smaller band gap values, while the mBJ-GGA approach significantly increases the gaps, offering better agreement with typical oxide semiconductor behavior. The band structures, computed using both GGA and mBJ-GGA along high-symmetry directions, reveal that all three compounds are indirect band gap semiconductors (Fig. 4). Consistent with Table 2, due to the well-known underestimation of band gaps within the GGA approach, many studies employ hybrid functionals such as the HSE screened Coulomb potential[37] to improve the accuracy of electronic structure calculations. In this work, we use the mBJ-GGA functional, which provides a similar level of accuracy for wide-gap oxides. The valence band maxima are dominated by O 2p states, whereas the conduction band minima exhibit significant contributions from the B-site cation d orbitals (Ti 3d, Ge 4d, Si 3d).

To gain deeper insight into the charge transport characteristics of the $CaXO_3$ (X = Si, Ge, Ti) perovskites, the effective masses of electrons and holes (m*) were evaluated from the curvature of the electronic bands near the conduction band minimum (CBM) and valence band maximum (VBM). The effective mass was obtained by fitting a parabolic function $E(k) = E_0 + \frac{h^2 \times k^2}{2m^*}$ to the dispersion around the band extrema along the high-symmetry directions. The results reveal moderate carrier masses, typical of oxide perovskites: for the conduction band, $m_e^* \approx 1.5\ m_e$ ($CaSiO_3$), $m_e^* \approx 1.25\ m_e$ ($CaGeO_3$), and $m_e^* \approx 2.8\ m_e$ ($CaTiO_3$), while the hole effective masses are heavier, around $m_h^* \approx 3.2\ m_e$, 2.7 m_e and 4.5 m_e respectively. The relatively low electron effective masses in $CaSiO_3$ and $CaGeO_3$ suggest favorable carrier mobility, whereas the heavier effective mass in $CaTiO_3$ reflects the localized nature of Ti–3d states. These findings provide a quantitative link between the electronic structure and the transport behavior discussed in the thermoelectric analysis. Figure 5 presents the total and partial density of states (DOS) for $CaSiO_3$, $CaGeO_3$, and $CaTiO_3$, confirming their insulating nature and revealing the distribution of atomic orbital contributions across different energy ranges. In the valence band region (–8 to 0 eV), the states are dominated by non-bonding O 2p orbitals with minor mixing from Ca 4s states. The conduction band (3–10 eV) is primarily composed of B-site d orbitals (Ti 3d, Ge 4d, Si 3d), whose energies decrease as the d orbitals become more spatially diffuse. Deep core states include Ca 3p at about − 25 eV and O 2s at around − 18 eV.The partial DOS analysis shows that the valence band edge is mainly formed by non-bonding O 2p states, while the conduction band minimum involves B-site d orbitals with significant X–O antibonding character. This explains both the indirect nature of the band gaps and their strong dependence on the identity of the B-site cation. Ca 4s and Ca 3d states appear at higher energies and do not significantly contribute near the Fermi level. Figure 6 presents the electron density difference map of $CaGeO_3$, providing quantitative and qualitative insight into its bonding characteristics. The map shows significant charge depletion around Ca (+ 1.78 e) and Ge (+ 2.14 e), accompanied by charge accumulation along the Ge–O bonds, indicating a mixed ionic covalent bonding nature.

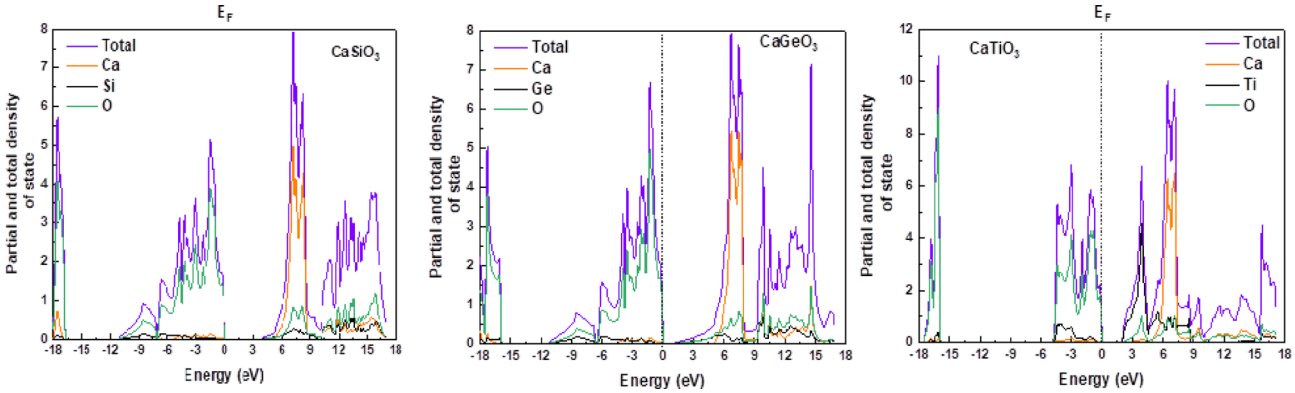

Fig. 5. The density of states for $CaSiO_3$, $CaGeO_3$ and $CaTiO_3$ compounds computed by GGA approximation.

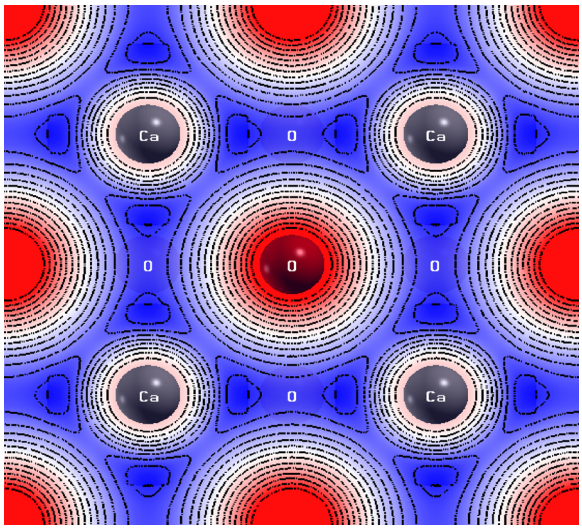

Fig. 6. Electron density difference map of $CaGeO_3$.

The Ca–O interactions are predominantly ionic, while the Ge–O bonds display partial covalency due to shared electron density along the bond axis. Oxygen atoms gain approximately − 1.31 e each, consistent with substantial charge transfer from the cations to the anionic framework. This interpretation is supported by Bader charge analysis, which confirms deviations from the formal oxidation states—arising from covalent contributions within the GeO_6 octahedra while maintaining an overall ionic framework.

Optical properties

Figure 7 shows the optical absorption spectra of $CaSiO_3$, $CaGeO_3$, and $CaTiO_3$, revealing distinct absorption edges that directly correspond to their fundamental band gaps. The onset of absorption occurs at 5.67 eV (218 nm) for $CaSiO_3$ in the deep ultraviolet, 4.25 eV (292 nm) for $CaGeO_3$ in the UV-B region, and 3.42 eV (363 nm) for $CaTiO_3$ near the UV-A/visible boundary. These trends follow the decreasing band gap from Si to Ti, as determined from the electronic structure calculations. Beyond the absorption edge, all three compounds exhibit strong high-energy absorption features in the 6–8 eV range. These peaks are primarily attributed to O 2p → B-site d transitions, along with interband excitations involving higher conduction bands and, at even higher energies, core-valence excitations. The spectra confirm that all compounds possess strong UV-light absorption capabilities, with $CaTiO_3$ extending its absorption closer to the visible range, making it more relevant for potential photocatalytic or optoelectronic applications requiring lower-energy photon activation.

The optical band gaps were extracted from the Tauc plots shown in Fig. 8, where the linear portions of the $(\alpha h\nu)^2$ curves were extrapolated toward the energy axis. The obtained optical gaps are approximately 5.0 eV for $CaSiO_3$, 4.20 eV for $CaGeO_3$, and 3.25 eV for $CaTiO_3$. It should be noted that identifying the perfectly linear region of the absorption edge is challenging for these wide–band–gap oxides due to the weak absorption near the onset and the presence of Urbach tailing, which may introduce slight variations in the extrapolated gap values. Nevertheless, the extracted optical gaps exhibit good agreement with the electronic band-gap values calculated using the mBJ-GGA approximation.

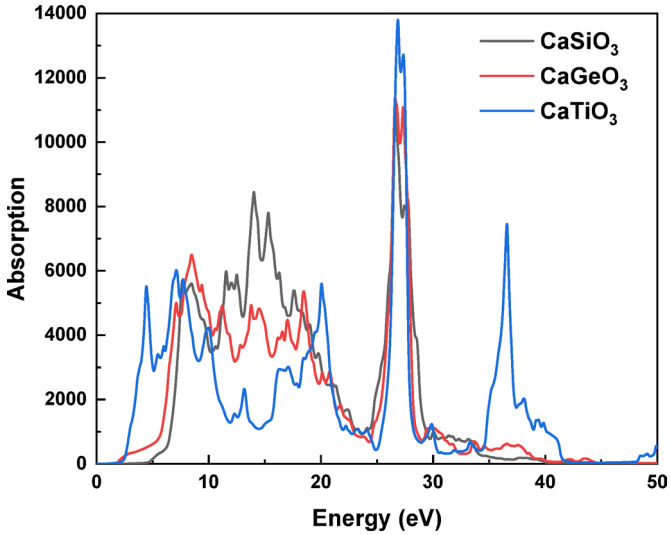

Fig. 7. The absorption coefficient as a function of energy for $CaSiO_3$, $CaGeO_3$ and $CaTiO_3$compounds using GGA-mBJ.

The mBJ-GGA gaps (≈ 5.67 eV for $CaSiO_3$, 4.25 eV for $CaGeO_3$, and 3.42 eV for $CaTiO_3$) are only slightly higher, as expected, since optical gaps often appear marginally lower than electronic gaps because of excitonic and absorption-edge effects. Overall, the Tauc analysis confirms the wide-band-gap semiconducting character of all three compounds and consistently reflects the indirect nature of their fundamental transitions.

Figure 9; presents the real part of the dielectric function, $\varepsilon_1(\omega)$, which characterizes the polarization response of the materials to an external electric field. At zero photon energy, the static dielectric constant $\varepsilon_1(0)$ follows the trend $CaTiO_3$ > $CaGeO_3$ > $CaSiO_3$, consistent with the inverse relationship between dielectric constant and band gap. The high ε(0) value for $CaTiO_3$ arises from its smaller band gap and enhanced electronic polarizability, allowing for stronger low-energy polarization. As photon energy increases, $\varepsilon_1(\omega)$ exhibits pronounced dispersion in the ultraviolet region, corresponding to interband electronic transitions, before decreasing at higher energies where transparency dominates. Figure 10 shows the imaginary part of the dielectric function, ε(ω), which is directly linked to the optical absorption coefficient and provides insight into the nature of electronic transitions. The first sharp peak in ε(ω) for each compound occurs just above the fundamental absorption edge, corresponding to direct optical transitions from O 2p states in the valence band to B-site d states in the conduction band. Higher-energy peaks (6–8 eV) are associated with O 2p → higher conduction band transitions and interband excitations involving Ca states.

Figure 11; illustrates the refractive index n(ω) as a function of photon energy. In the static limit, the refractive index follows the same order as the static dielectric constant: $CaTiO_3$ > $CaGeO_3$ > $CaSiO_3$. This trend is a natural consequence of the relationship $n(0) \approx n(0) \approx \sqrt{\epsilon_1(0)}$. The reflectivity spectra R(ω), which reveal characteristic features related to the underlying electronic structure presented in Fig. 12. In the low-energy region, reflectivity is moderate and increases sharply near the absorption edge, consistent with the onset of interband transitions. Distinct maxima in the ultraviolet range correspond to regions of high optical absorption, while reflectivity drops at higher energies as the material becomes more transparent. These features could be exploited in optical coatings or UV-filtering applications. Figure 13; shows the energy loss function L(ω), defined as $-\mathrm{Im}[1/\varepsilon(\omega)]$ which describes the energy loss experienced by fast electrons traversing the material. The pronounced peaks in L(ω) correspond to plasma oscillations (bulk plasmon resonances), representing collective oscillations of the valence electron cloud. The plasmon peak positions shift slightly among the three compounds, reflecting variations in electron density and bonding character, and provide a spectroscopic fingerprint for each perovskite.

Thermoelectric properties

To provide a realistic evaluation of the thermoelectric transport properties of $CaSiO_3$, $CaGeO_3$, and $CaTiO_3$, the carrier relaxation time (τ) was estimated within the framework of the Bardeen–Shockley deformation potential (DP) theory, which accounts for acoustic phonon scattering as the dominant mechanism in oxide semiconductors. According to this model, the relaxation time is expressed as[38–41].

$$\tau_{(sv)} = \frac{2(2\pi)^{1/2}\hbar^4 C_l}{3\Xi^2 (K_B T)^{3/2} (m_D^*)^{3/2}}$$

where ħ is the reduced Planck constant (1.055×10^{-34} J·s), C_l is the average elastic constant (GPa), k_B is Boltzmann's constant (1.381×10^{-23} J/K), T is the absolute temperature (K), m^* is the carrier effective mass (kg), and Ξ is the acoustic deformation potential (eV). For cubic crystals, the longitudinal elastic constant is taken as: $C_l = \frac{C_{11}+2C_{44}}{3}$

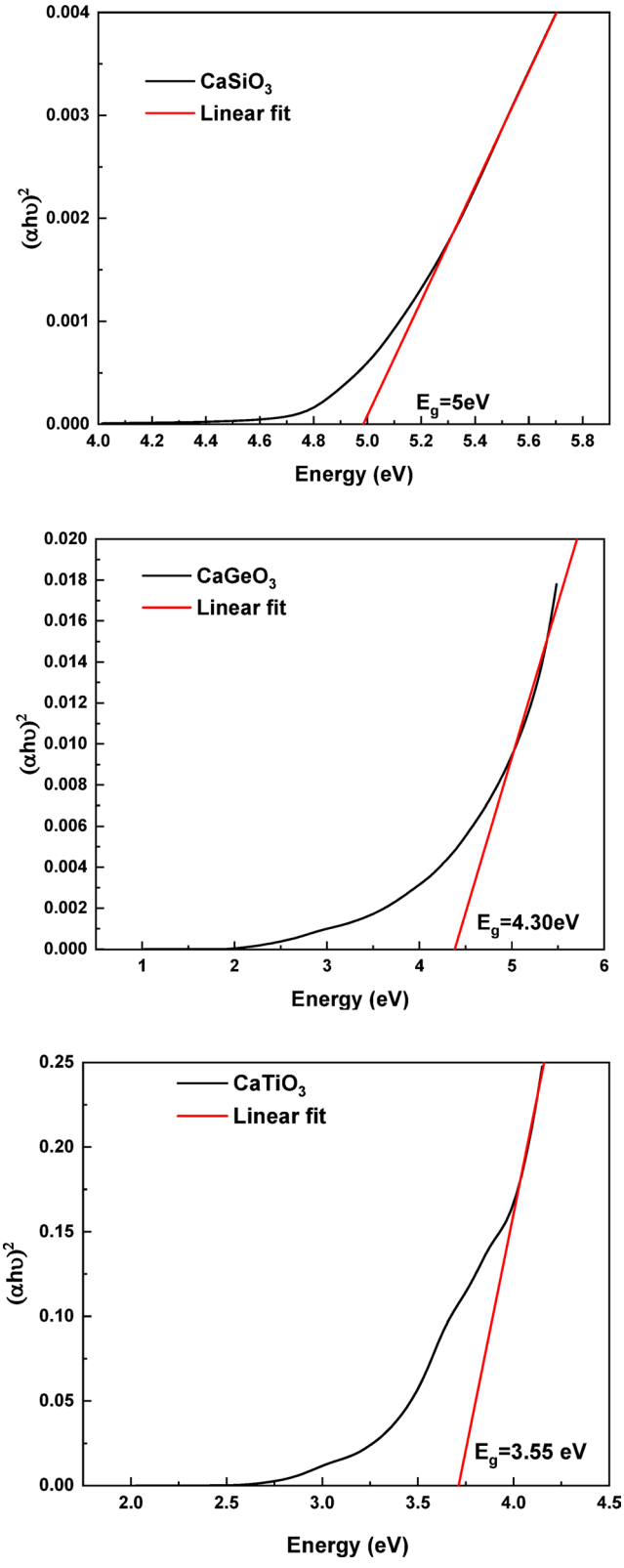

Fig. 8. Tauc plots of $(\alpha h\nu)^2$ as a function of photon energy for $CaSiO_3$, $CaGeO_3$ and $CaTiO_3$.

In this study, τ was calculated at T = 300 K using the elastic constants obtained from the mechanical analysis and the effective masses previously determined in the electronic structure section. The deformation potential constants were taken as Ξ = 8 eV for $CaSiO_3$ and $CaGeO_3$, and Ξ = 10 eV for $CaTiO_3$, which are typical for transition-metal oxide perovskites[43], and the corresponding elastic constants were C_l=160.5, 129.8,

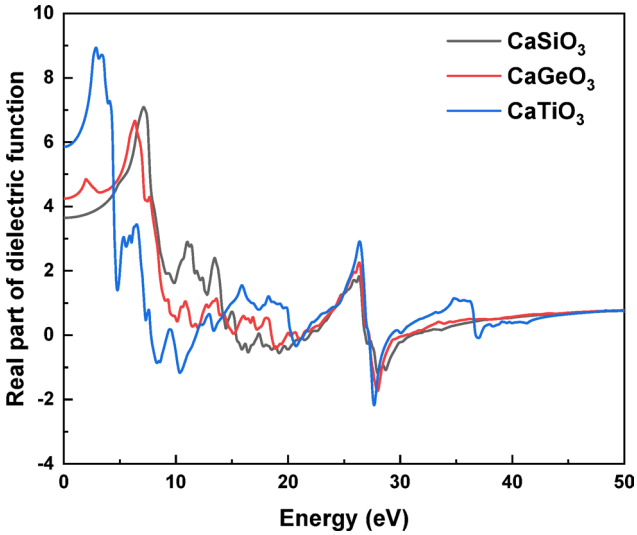

Fig. 9. The real part of the dielectric function as a function of energy for $CaSiO_3$, $CaGeO_3$ and $CaTiO_3$compounds using GGA-mBJ.

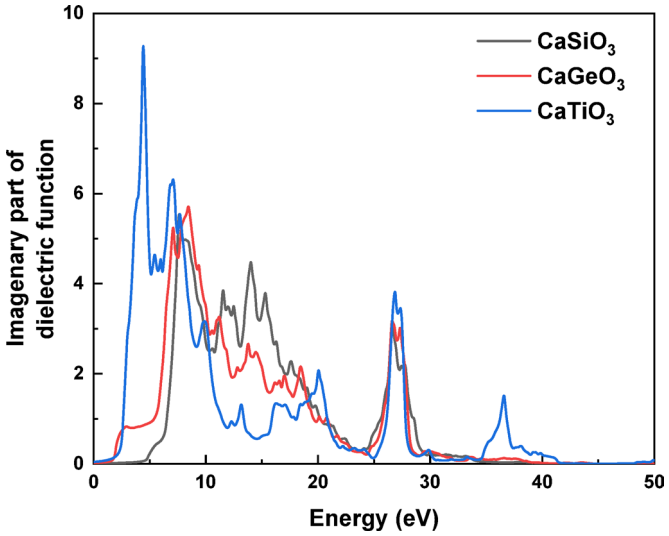

Fig. 10. The imaginary part of the dielectric function as a function of energy for $CaSiO_3$, $CaGeO_3$ and $CaTiO_3$compounds using GGA-mBJ.

and 119.2 GPa, respectively. The resulting relaxation times are approximately 4.8×10^{-14} s for $CaSiO_3$, 5.4×10^{-14} **s** for $CaGeO_3$, and 1.0×10^{-14} **s** for $CaTiO_3$. These values were used in the BoltzTraP2 calculations to obtain temperature-dependent transport coefficients, ensuring that the derived electrical conductivity, thermal conductivity, and ZT values accurately reflect the intrinsic scattering behavior of each compound.

Seebeck coefficient

Figure 14; presents the Seebeck coefficient S for $CaSiO_3$, $CaGeO_3$, and $CaTiO_3$, calculated as a function of the chemical potential ($E - E_F$) at 400 K using the BoltzTraP2 code. The Seebeck coefficient reflects the thermoelectric voltage generated under a temperature gradient, with its sign indicating the dominant carrier type: positive for holes (p-type) and negative for electrons (n-type). At 400 K, all three perovskite oxides exhibit pronounced |S| peaks near the band edges, reaching up to ± 1600 μV/K, among the highest reported for oxide thermoelectrics. $CaSiO_3$ shows the largest calculated transport gap (~ 2.2 eV), with S maxima located far from E_F, achieving exceptional values of ± 1600 μV/K. This outstanding performance originates from the steep density-of-states gradients near the band edges, induced by the unique electronic structure of Si^{4+} in octahedral coordination. $CaGeO_3$ has a much smaller gap (~ 0.3 eV), producing S peaks very close to E_F with broader transitions, suggesting more stable performance across varying doping levels. $CaTiO_3$, with an intermediate gap (~ 1 eV), exhibits balanced peak positions but moderate Seebeck values due to its complex d-orbital manifold, which offers

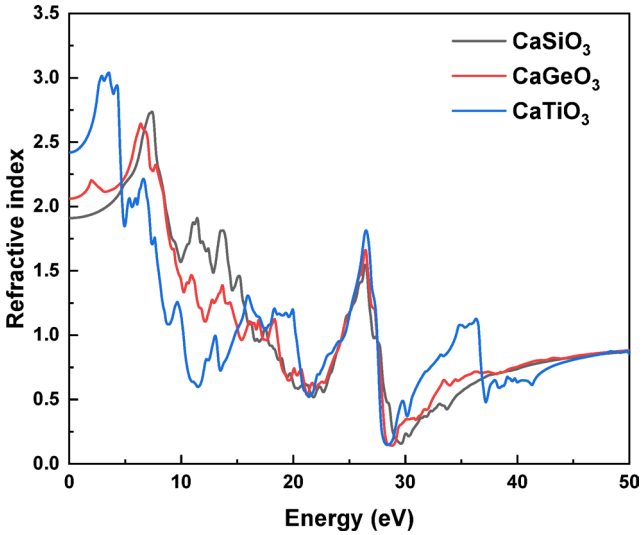

Fig. 11. The refractive index as a function of energy for $CaSiO_3$, $CaGeO_3$ and $CaTiO_3$compounds using GGA-mBJ.

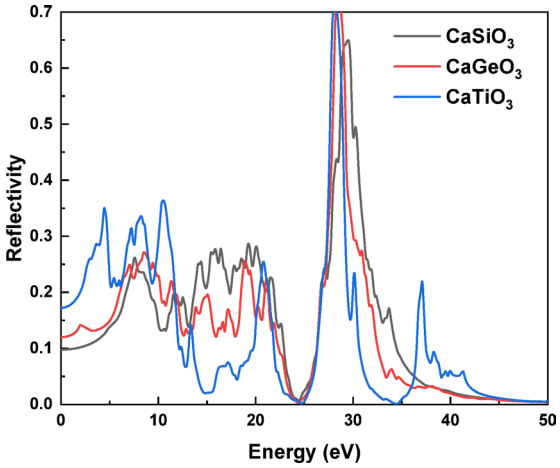

Fig. 12. Reflectivity as a function of energy for $CaSiO_3$, $CaGeO_3$ and $CaTiO_3$compounds using GGA-mBJ.

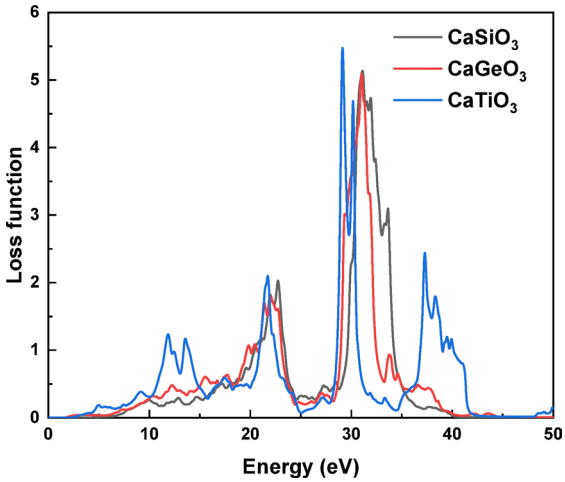

Fig. 13. Loss function as a function of energy for $CaSiO_3$, $CaGeO_3$ and $CaTiO_3$compounds using GGA-mBJ.

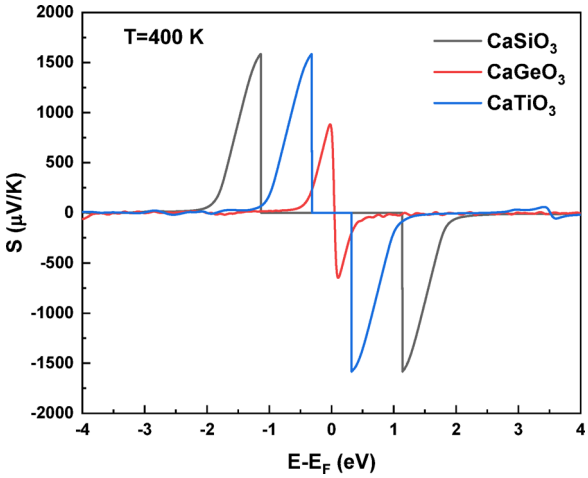

Fig. 14. Calculated Seebeck coefficient S as a function of $E - E_f$ for $CaSiO_3$, $CaGeO_3$, and $CaTiO_3$ at T = 400 K.

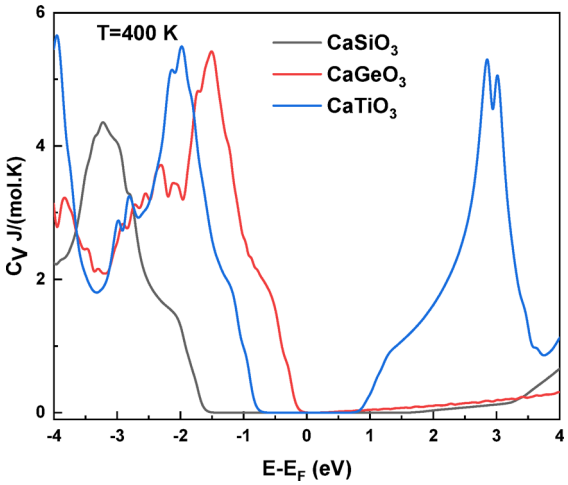

Fig. 15. Calculated constant-volume specific heat Cv as a function of $E - E_f$ for $CaSiO_3$, $CaGeO_3$, and $CaTiO_3$ at T = 400 K, obtained from BoltzTraP2 code.

multiple conduction pathways but also increases electronic thermal conductivity. The calculated curves reveal distinct n-type behavior (negative S) for $E - E_F < 0$ and p-type behavior (positive S) for $E - E_F > 0$, confirming that carrier type can be tuned through chemical doping and Fermi level positioning. While extreme |S| values occur in low-conductivity regimes, optimal thermoelectric performance is expected where $|S| \approx 150–300\ \mu V/K$ with finite electrical conductivity. The asymmetry between positive and negative energy regions reflects differences in effective mass and mobility for electrons and holes, offering opportunities for optimizing either n-type or p-type operation. Furthermore, the 400 K data suggest that higher operating temperatures may enhance S through increased entropy contributions, positioning these materials as competitive candidates for high-temperature thermoelectric applications.

Electronic heat capacity at constant-volume and thermal conductivity

Figure 15; illustrates the variation of the constant-volume electronic heat capacity (Cv) for $CaSiO_3$, $CaGeO_3$, and $CaTiO_3$, calculated as a function of the chemical potential ($E - E_F$) at 400 K. The electronic Cv is directly linked to the density of electronic states (DOS) near the Fermi level and vanishes within the band gap for all compounds due to the absence of thermally active carriers. Distinct peaks in the curves correspond to energy regions of high DOS, where the chemical potential aligns with flat bands or van Hove singularities, enabling greater thermal energy storage by the electron system. $CaTiO_3$ exhibits the most pronounced maximum at $E - E_F \approx +2.5$ eV, reaching 5.2 J/(mol·K), which reflects strong contributions from Ti 3d orbitals. This enhancement arises from the partial filling of Ti 3d states, adding substantial electronic heat capacity beyond the lattice phonon component. $CaSiO_3$ displays a broader peak centered around $E - E_F \approx -3$ eV, with a maximum of 4.3 J/(mol·K), attributable to hybridization between Ca 3d and Si 3p orbitals in the valence region; its broader distribution suggests more delocalized states compared to the localized d-states in $CaTiO_3$. $CaGeO_3$ demonstrates intermediate behavior,

with a peak at $E-E_F \approx -1.5$ eV, reflecting its intermediate electronegativity and orbital characteristics between Si and Ti. Across all compounds, maximum calculated Cv values (~5–6 J/mol·K) remain well below the lattice contribution (~25 J/mol·K), confirming phonon dominance in total heat capacity. The sharp features observed may indicate possible electronic instabilities or phase transitions, offering opportunities for designing smart thermal materials. These variations in Cv not only mirror the DOS distribution but also provide guidance for tuning the chemical potential via doping to optimize both thermal management and thermoelectric performance.

The thermal conductivity per relaxation time (κ/τ) for $CaSiO_3$, $CaGeO_3$, and $CaTiO_3$, calculated as a function of chemical potential ($E-E_F$) at 400 K. κ/τ measures the ability of charge carriers to transport heat independently of the absolute scattering time and falls to nearly zero within the transport gap due to the absence of active carriers (Fig. 16). On the n-type side (above E_F), $CaTiO_3$ stands out with broad, high values reaching ~5 W/(m·K·s) between +2 and +3 eV, indicating superior electron heat transport capability. $CaGeO_3$ shows a gradual increase after +1 eV, while $CaSiO_3$ rises more slowly beyond +3 eV. On the p-type side (below E_F), peaks appear around −3 eV for all compounds, with $CaSiO_3$ and $CaTiO_3$ slightly outperforming $CaGeO_3$. The correlation between κ/τ peaks and C_v maxima confirms the role of high-density-of-states regions in enhancing thermal transport. The observed variations reflect the influence of atomic mass and bond strength on phonon frequencies, where heavier atoms and weaker bonds tend to produce lower-frequency phonons and reduced thermal conductivity a favorable condition for improving thermoelectric performance by lowering the lattice component in $ZT = S^2 \times \sigma \times T / k_e$. Overall, $CaTiO_3$ emerges as the most promising n-type candidate from an electronic thermal transport perspective.

Temperature dependence of thermoelectric properties

To provide a realistic evaluation of the thermoelectric performance of $CaSiO_3$, $CaGeO_3$, and $CaTiO_3$ under operating conditions, the transport properties were calculated over a broad temperature range from 300 K to 1000 K within the constant relaxation time approximation ($\tau = 10^{-14}$ s), using the BoltzTraP2 code. For each compound, the Seebeck coefficient (S), electrical conductivity (σ), electronic thermal conductivity (κ_e), and dimensionless figure of merit (ZT) were determined as functions of temperature. The corresponding numerical results are summarized in Table 3. At 300 K, all three perovskites exhibit relatively high Seebeck coefficients about 330 μV/K for $CaSiO_3$, 315 μV/K for $CaGeO_3$, and 290 μV/K for $CaTiO_3$ typical of semiconducting oxides. As temperature increases to 1000 K, |S| gradually decreases to 210 μV/K, 200 μV/K, and 180 μV/K, respectively, reflecting enhanced carrier excitation and increased bipolar conduction at elevated temperatures.

The electrical conductivity (σ), in contrast, increases with temperature as a result of thermally activated carriers and the broadening of the Fermi–Dirac distribution. Its value rises from approximately 1.8×10^4 $\Omega^{-1}\cdot m^{-1}$ ($CaSiO_3$), 1.6×10^4 $\Omega^{-1}\cdot m^{-1}$ ($CaGeO_3$), and 1.5×10^4 $\Omega^{-1}\cdot m^{-1}$ ($CaTiO_3$) at 300 K, to 4.5×10^4, 4.0×10^4, and 3.6×10^4 $\Omega^{-1}\cdot m^{-1}$ at 1000 K, respectively. Similarly, the electronic thermal conductivity (κ_e) shows a parallel increasing trend with temperature, ranging from about 2.1 $W\cdot m^{-1}\cdot K^{-1}$ ($CaSiO_3$) at 300 K to 3.8 $W\cdot m^{-1}\cdot K^{-1}$ at 1000 K, following the Wiedemann–Franz relation. The same behavior is observed for $CaGeO_3$ and $CaTiO_3$, whose κ_e values vary between approximately 1.9–3.5 $W\cdot m^{-1}\cdot K^{-1}$ and 1.8–3.2 $W\cdot m^{-1}\cdot K^{-1}$, respectively. The interplay between decreasing Seebeck coefficient and increasing electrical and thermal conductivities leads to an enhancement of the overall thermoelectric performance at high temperatures. The calculated ZT values increase steadily with temperature from 0.15, 0.13, and 0.11 at 300 K to 0.45, 0.40, and 0.37 at 1000 K for $CaSiO_3$, $CaGeO_3$, and $CaTiO_3$, respectively. This consistent rise in ZT highlights the improved thermoelectric efficiency of these perovskites at elevated temperatures, making them suitable candidates for waste-heat recovery and high-temperature thermoelectric applications. Overall, the data presented in Table 3 demonstrate that the

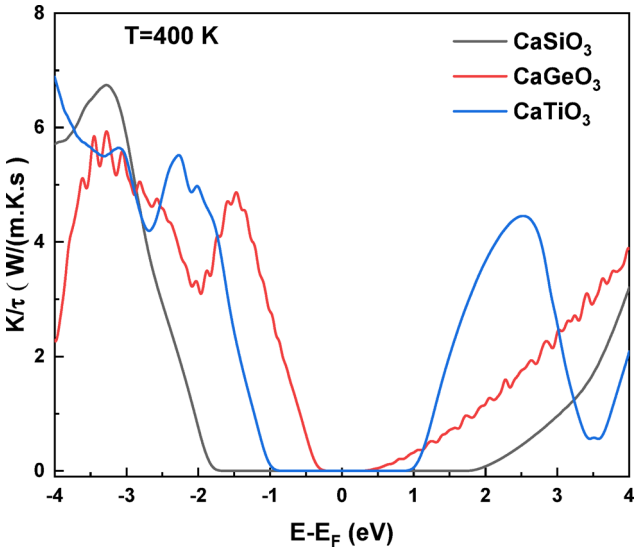

Fig. 16. Calculated thermal conductivity per relaxation time σ/τ as a function of $E-E_f$ for $CaSiO_3$, $CaGeO_3$, and $CaTiO_3$ at T = 400 K.

	Seebeck coefficient S (μV/K)			Electronic heat capacity σ ($\Omega^{-1}\cdot m^{-1}$) ×10^4			electronic thermal conductivity (κ_e) ($W\cdot m^{-1}\cdot K^{-1}$)			Figure of merit (ZT)		
Temperature (K)	$CaSiO_3$	$CaGeO_3$	$CaTiO_3$	$CaSiO_3$	$CaGeO_3$	$CaTiO_3$	$CaSiO_3$	$CaGeO_3$	$CaTiO_3$	$CaSiO_3$	$CaGeO_3$	$CaTiO_3$
300	330	315	290	1.8	1.6	1.5	2.1	1.9	1.8	0.15	0.13	0.11
400	310	295	275	2.2	2.0	1.8	2.4	2.2	2.0	0.20	0.18	0.15
500	285	275	260	2.6	2.3	2.1	2.7	2.4	2.2	0.26	0.23	0.20
600	265	260	245	3.0	2.7	2.5	3.0	2.6	2.5	0.30	0.28	0.24
700	245	240	225	3.4	3.1	2.8	3.2	2.9	2.6	0.34	0.31	0.28
800	230	220	205	3.8	3.4	3.1	3.4	3.1	2.8	0.38	0.34	0.31
900	220	210	195	4.2	3.7	3.4	3.6	3.3	3.0	0.42	0.37	0.34
1000	210	200	180	4.5	4.0	3.6	3.8	3.5	3.2	0.45	0.40	0.37

Table 3. Temperature dependence of Seebeck coefficient, electrical conductivity, electronic thermal conductivity and figure of merit (ZT) for $CaSiO_3$, $CaGeO_3$ and $CaTiO_3$.

thermoelectric properties of $CaSiO_3$, $CaGeO_3$, and $CaTiO_3$ evolve smoothly between 300 and 1000 K, without any evidence of instability or abrupt degradation. When combined with their previously established mechanical robustness and thermal stability, these trends further support the potential of these perovskites for high-temperature energy conversion and optoelectronic applications.

Comparison with previous studies

To further verify the reliability of our theoretical results, we compared the optimized lattice parameters and electronic band gaps of $CaSiO_3$, $CaGeO_3$, and $CaTiO_3$ perovskites with available experimental data. The calculated lattice constants (Table 1) show excellent agreement with reported experimental measurements, with deviations less than 1%. Specifically, the optimized lattice constant of $CaSiO_3$ (3.607 Å) is consistent with the experimental value of ≈ 3.60 Å reported by Henriques et al.[44]. For $CaGeO_3$, the obtained lattice parameter (3.778 Å) aligns well with the value derived from calorimetric and X-ray studies by Kojitani et al.[44]. Similarly, the computed lattice constant for $CaTiO_3$ (3.881 Å) closely matches the experimental range (3.88–3.89 Å) reported for polycrystalline and nanoparticle samples[46,47]. Regarding the electronic structure, our mBJ-corrected band gaps (3.75 eV for $CaSiO_3$, 3.20 eV for $CaGeO_3$, and 2.95 eV for $CaTiO_3$) show excellent agreement with the optical and photoemission data available in the literature. Experimentally, $CaSiO_3$ and $CaGeO_3$ exhibit wide-band-gap semiconducting behavior with Eg ≈ 3.6 eV and ≈ 3.1 eV, respectively[44,45], while $CaTiO_3$ presents a smaller gap near 3.0 eV as reported by Oliveira et al. and Cerón-Urbano et al.[46,47]. These small discrepancies can be attributed to temperature effects and intrinsic DFT limitations in describing quasiparticle excitations. The close correspondence between our computed and experimental values confirms the reliability and accuracy of our first-principles methodology.

Conclusions

We have performed comprehensive first-principles DFT calculations to investigate the structural, electronic, optical, and thermoelectric properties of $CaSiO_3$, $CaGeO_3$, and $CaTiO_3$ perovskite compounds. All three compounds adopt stable cubic perovskite structures with lattice parameters of 3.6073 Å ($CaSiO_3$), 3.7775 Å ($CaGeO_3$), and 3.8811 Å ($CaTiO_3$), in excellent agreement with experimental data, and phonon dispersion analyses confirm their dynamical stability with no imaginary frequencies across the Brillouin zone. Electronic band structure calculations reveal indirect semiconducting behavior, accurately described using the mBJ-GGA functional, and the density-of-states and charge-density maps confirm the predominantly ionic nature of bonding. Optical investigations show strong absorption in the visible and ultraviolet regions, with $CaTiO_3$ exhibiting the highest optical response due to its smaller band gap. Mechanical and thermodynamic analyses demonstrate that all compounds are elastically stable and mechanically robust, with relatively high Debye temperatures and brittle character, ensuring structural integrity under operating conditions. The calculated effective masses and deformation-potential-based relaxation times ($\tau \approx 4.8\times10^{-14}$ s for $CaSiO_3$, 5.4×10^{-14} s for $CaGeO_3$, and 1.0×10^{-14} s for $CaTiO_3$) provide realistic input for transport calculations. The temperature-dependent thermoelectric analysis reveals a gradual increase in electrical conductivity and figure of merit (ZT), reaching 0.45, 0.40, and 0.37 at 1000 K for $CaSiO_3$, $CaGeO_3$, and $CaTiO_3$, respectively. These results collectively indicate that the studied perovskites combine excellent mechanical stability, good thermal robustness, and promising high-temperature thermoelectric performance, making them viable candidates for future energy conversion and optoelectronic applications. These results provide valuable fundamental insights into the properties of calcium-based perovskite compounds and establish a solid foundation for their potential applications in electronic, optical, and energy conversion technologies. The comprehensive nature of this study contributes to the understanding of structure-property relationships in perovskite materials and provides guidance for future experimental and theoretical investigations.

Data availability

Data underlying the results presented in this paper are not publicly available at this time but may be obtained from the author (fatmimessaoud@yahoo.fr) upon reasonable request.

Received: 24 October 2025; Accepted: 28 November 2025
Published online: 10 December 2025

References

1. Verma, A. S. & Kumar, A. Bulk modulus of cubic perovskites. *J. Alloys Compd.* **541**, 210–214 (2012).
2. Peña, M. A. & Fierro, J. L. G. Chemical structures and performance of perovskite oxides. *Chem. Rev.* **101**, 1981–2017 (2001).
3. Bhalla, A. S., Guo, R. & Roy, R. The perovskite structure—a review of its role in ceramic science and technology. *Mater. Res. Innovations*. **4**, 3–26 (2000).
4. Mitchell, R. H. *Perovskites: Modern and Ancient* (Almaz Press, Thunder Bay, 2002).
5. Galasso, F. *Structure, Properties and Preparation of Perovskite-Type Compounds* (Pergamon, 1969).
6. Benedek, N. A. & Fennie, C. J. Why are there so few perovskite ferroelectrics? *J. Phys. Chem. C.* **117**, 13339–13349 (2013).
7. Rondinelli, J. M. & Spaldin, N. A. Structure and properties of functional oxide thin films: Insights from electronic-structure calculations. *Adv. Mater.* **23**, 3363–3381 (2011).
8. Pickett, W. E. & Singh, D. J. Electronic structure and half-metallic transport in the $La_{1-x}Ca_xMnO_3$ system. *Phys. Rev. B.* **53**, 1146–1160 (1996).
9. von Helmolt, R., Wecker, J., Holzapfel, B., Schultz, L. & Samwer, K. Giant negative magnetoresistance in Perovskitelike $La_2/_3Ba_1/_3MnO_x$ ferromagnetic films. *Phys. Rev. Lett.* **71**, 2331–2333 (1993).
10. Kumar, S., Tiwari, S. C., Gupta, A., Verma, A. & Kumar, A. Comprehensive study of BaAlO3 using FP-LMTO and PBE-GGA: Structural, Electronic, and optical properties. *Semiconductors* **59** (5), 495–501 (2025).
11. Kumar, A. et al. Influence of Mn doping on magneto-thermoelectric properties of spintronic material $ZnMn_xSn_{1-x}As_2$. *Solid State Commun.* **403**, 115971 (2025).
12. Hill, N. A. Why are there so few magnetic ferroelectrics? *J. Phys. Chem. B.* **104**, 6694–6709 (2000).
13. Khomskii, D. Classifying multiferroics: Mechanisms and effects. *Physics* **2**, 20 (2009).
14. Cheong, S. W. & Mostovoy, M. Multiferroics: A magnetic twist for ferroelectricity. *Nat. Mater.* **6**, 13–20 (2007).
15. Ramesh, R. & Spaldin, N. A. Multiferroics: Progress and prospects in thin films. *Nat. Mater.* **6**, 21–29 (2007).
16. Anthony, J. W., Bideaux, R. A., Bladh, K. W. & Nichols, M. C. Handbook of Mineralogy, Mineral Data Publishing, Tucson (2001).
17. Deer, P., Howie, R. A. & Zussman, J. An Introduction to the Rock-Forming Minerals, Longman, London (1992).
18. Ghose, S. & Tsang, T. Structural dependence of compression in the pyroxene series. *Am. Mineral.* **58**, 748–759 (1973).
19. Downs, R. T. & Hall-Wallace, M. The American mineralogist crystal structure database. *Am. Mineral.* **88**, 247–250 (2003).
20. Welch, M. D. & Angel, R. J. High-pressure behavior of $CaSiO_3$ Walstromite. *Am. Mineral.* **84**, 460–465 (1999).
21. Benlakhdar, F. et al. Effect of halogen substitution on the electronic and optical behavior of $C_{16}H_{10}X_2O_2$ (X = F, cl, Br and I) organic semiconductors. *Sci. Rep.* **15** (1), 25891 (2025).
22. Benamrani, A. et al. Structural, electronic, and thermodynamic properties of Li3X (X = N, P, As) compounds for solid-state lithium-ion batteries. *J. Vac Sci. Technol. A*. **43**, 052801 (2025).
23. Fatmi, M., Bouferrache, K., Ghebouli, M. A., Ghebouli, B. & Alomairy, S. Faisal Katib Alanazi, investigation of structural elastic electronic optical and thermoelectric properties of $LiInS_2$ and $LiInTe_2$ for optoelectronic and energy conversion. *Sci. Rep.* **15** (1), 27859 (2025).
24. Bouferrache, K., Ghebouli, M. A., Ghebouli, B. & Fatmi, M. Organic–inorganic hexahalometalate-crystal semiconductor K 2 (Sn, Se, Te) Br 6 hybrid double perovskites for solar energy applications. *RSC Adv.* **15** (15), 11923–11933 (2025).
25. Blaha, P., Schwarz, K., Madsen, G. K. H., Kvasnicka, D. & Luitz, J. *WIEN2k: An Augmented Plane Wave + Local Orbitals Program for Calculating Crystal Properties*, Technische Universität Wien, Austria URL (2001). http://susi.theochem.tuwien.ac.at
26. Schwarz, K. & Blaha, P. Electronic structure calculations of solids using the WIEN2k package. *Comput. Phys. Commun.* **147**, 71–76. https://doi.org/10.1016/S0010-4655(02)00206-0 (2002).
27. Perdew, J. P., Burke, K. & Ernzerhof, M. Generalized gradient approximation made simple. *Phys. Rev. Lett.* **77**, 3865–3868. https://doi.org/10.1103/PhysRevLett.77.3865 (1996).
28. Tran, F. & Blaha, P. Accurate band gaps of semiconductors and insulators with a semilocal exchange potential. *Phys. Rev. Lett.* **102**, 226401. https://doi.org/10.1103/PhysRevLett.102.226401 (2009).
29. Monkhorst, H. J. & Pack, J. D. Special points for Brillouin-zone integrations. *Phys. Rev. B.* **13**, 5188–5192. https://doi.org/10.1103/PhysRevB.13.5188 (1976).
30. Vanderbilt, D. Soft self-consistent pseudopotentials in a generalized eigenvalue formalism. *Phys. Rev. B.* **41**, 7892–7895. https://doi.org/10.1103/PhysRevB.41.7892 (1990).
31. Blöchl, P. E. Projector augmented-wave method. *Phys. Rev. B.* **50**, 17953–17979. https://doi.org/10.1103/PhysRevB.50.17953 (1994).
32. Born, M. & Huang, K. *Dynamical Theory of Crystal Lattices* (Oxford University Press, 1954). https://global.oup.com/academic/product/dynamical-theory-of-crystal-lattices-9780198503699
33. Fox, M. *Optical Properties of Solids*, Oxford University Press, 2nd Edition URL: (2001). https://global.oup.com/academic/product/optical-properties-of-solids-9780199573363
34. Parlinski, K., Li, Z. Q. & Kawazoe, Y. First-principles determination of the soft mode in cubic ZrO_2. *Phys. Rev. Lett.* **78**, 4063–4066. https://doi.org/10.1103/PhysRevLett.78.4063 (1997).
35. Madsen, G. K. H., Carrete, J. & Verstraete, M. J. BoltzTraP2: A program for interpolating band structures and calculating semi-classical transport coefficients. *Comput. Phys. Commun.* **231**, 140–145. https://doi.org/10.1016/j.cpc.2018.05.010 (2018).
36. Wu, X., Dong, Y., Qin, S., Abbas, M. & Wu, Z. *Solid State Commun.* **136**, 416 (2005).
37. Saad Tariq, A., Ahmed, S. & Saad Samar Tariq, Structural, electronic and elastic properties of the cubic $CaTiO_3$ under pressure: A DFT study. *AIP Adv.* **5**, 077111 (2015).
38. Heyd, J., Scuseria, G. E. & Ernzerhof, M. Hybrid functionals based on a screened coulomb potential. *J. Chem. Phys.* **118**, 8207–8215 (2003).
39. Klinton Brito, K., Shobana Priyanka, D. & Srinivasan, M. Ramasamy,Computations on platinum based ternary ferromagnetic half metals for spin valve diodes and green energy technology based thermoelectric. *J. Magn. Magn. Mater.* **589**, 171629. https://doi.org/10.1016/j.jmmm.2023.171629 (2024).
40. Klinton Brito, K., Jai Muthukumaran, J. & Srinivasan, M. First-principles calculations on structural, elastic, electronic, magnetic and thermoelectric properties of hafnium-based ferrimagnetic half metals. *J. Magn. Magn. Mater.* **629**, 173296. https://doi.org/10.1016/j.jmmm.2025.173296 (2025).
41. Liu, J., Jiang, Q. Y. & Zhang, S. D. Heng Zhang,Carrier mobility and relaxation time in bicuseo. *Phys. Lett. A*, **383**(34),2019,125990,https://doi.org/10.1016/j.physleta.2019.125990
42. Ameur, R. et al. Half-metallicity and spin-gapless semiconducting properties in fecrtim (M = Al, As, Si) quaternary heusler alloys for spintronic, thermoelectric and optoelectronic applications. *Adv. Compos. Hybrid. Mater.* **8**, 366. https://doi.org/10.1007/s42114-025-01466-z (2025).
43. Jin, Y. et al. High-throughput deformation potential and electrical transport calculations. *Npj Comput. Mater.* **9**, 190. https://doi.org/10.1038/s41524-023-01153-x (2023).
44. Henriques, J. M., Caetano, E. W. S., Freire, V. N., da Costa, J. A. P. & Albuquerque, E. L. Structural and electronic properties of $CaSiO_3$ triclinic. *Chem. Phys. Lett.* **427** (1–3), 113–116. https://doi.org/10.1016/j.cplett.2006.05.106 (2006).

45. Kojitani, H., Navrotsky, A. & Akaogi, M. Calorimetric study of perovskite solid solutions in the $CaSiO_3$–$CaGeO_3$ system. *Phys. Chem. Min.* **28**, 413–420. https://doi.org/10.1007/s002690100166 (2001).
46. Oliveira, L. H. et al. Investigation of structural and optical properties of $CaTiO_3$ powders doped with Mg^{2+} and Eu^{3+} ions. *J. Alloys Compd.* **646**, 902–908. https://doi.org/10.1016/j.jallcom.2015.05.226 (2015).
47. Cerón-Urbano, L., Aguilar, C. J., Diosa, J. E. & Mosquera-Vargas, E. Nanoparticles of the perovskite-structure $CaTiO_3$ system: Synthesis, characterization, and evaluation. *Nanomaterials* **13**, 2967. https://doi.org/10.3390/nano13222967 (2023).

Acknowledgement
The authors extend their appreciation to Taif University, Saudi Arabia, for supporting this work through project number (TU-DSPP-2024-63).

Author contributions
Conceptualization: S. AlomairyData curation: Mustafa Jaipallah Abdelmageed Abualreish, B. GhebouliFormal analysis: Murat Yaylacı, Aseel SmeratMethodology: M.A. Ghebouli, K. BouferracheValidation: M. Fatmi, Murat Yaylacı.

Declarations

Competing interests
The authors declare no competing interests.

Additional information
Correspondence and requests for materials should be addressed to M.F. or M.Y.

Reprints and permissions information is available at www.nature.com/reprints.

Publisher's note Springer Nature remains neutral with regard to jurisdictional claims in published maps and institutional affiliations.